Optical observations and modeling of the superluminous supernova 2018lfe

Yin, Y.; Gomez, S.; Berger, E.; Hosseinzadeh, G.; Nicholl, M.; Blanchard, P.K.

DOI:
10.3847/1538-4357/ac6183

Document Version
Publisher's PDF, also known as Version of record

Citation for published version (Harvard):
Yin, Y, Gomez, S, Berger, E, Hosseinzadeh, G, Nicholl, M & Blanchard, PK 2022, 'Optical observations and modeling of the superluminous supernova 2018lfe', *The Astrophysical Journal*, vol. 931, no. 1, 32. https://doi.org/10.3847/1538-4357/ac6183

The Astrophysical Journal, 931:32 (9pp), 2022 May 20 https://doi.org/10.3847/1538-4357/ac6183

Optical Observations and Modeling of the Superluminous Supernova 2018lfe

Yao Yin[1], Sebastian Gomez[1,2], Edo Berger[1], Griffin Hosseinzadeh[1,3], Matt Nicholl[4], and Peter K. Blanchard[5]
[1] Center for Astrophysics | Harvard & Smithsonian, 60 Garden Street, Cambridge, MA 02138, USA; yyin@college.harvard.edu
[2] Space Telescope Science Institute, 3700 San Martin Drive, Baltimore, MD 21218, USA
[3] Steward Observatory, University of Arizona, 933 N. Cherry Avenue, Tucson, AZ 85721, USA
[4] Birmingham Institute for Gravitational Wave Astronomy and School of Physics and Astronomy, University of Birmingham, Birmingham B15 2TT, UK
[5] Center for Interdisciplinary Exploration and Research in Astrophysics and Department of Physics and Astronomy, Northwestern University, 1800 Sherman Avenue, Evanston, IL 60201, USA
Received 2021 September 11; revised 2022 March 15; accepted 2022 March 19; published 2022 May 20

Abstract

We present optical imaging and spectroscopy of SN 2018lfe, which we classify as a Type I superluminous supernova (SLSN-I) at a redshift of $z = 0.3501 \pm 0.0004$ with a peak absolute magnitude of $M_r = -22.1 \pm 0.1$ mag, one of the brightest SLSNe discovered. SN 2018lfe was identified for follow-up using our FLEET machine-learning pipeline. Both the light curve and the spectra of SN 2018lfe are consistent with the broad population of SLSNe. We fit the light curve with a magnetar central engine model and find an ejecta mass of $M_{\rm ej} \approx 3.8\ M_\odot$, a magnetar spin period of $P \approx 2.9$ ms, and a magnetic field strength of $B_\perp \approx 2.8 \times 10^{14}$ G. The magnetic field strength is near the top of the distribution for SLSNe, while the spin period and ejecta mass are near the median values of the distribution for SLSNe. From late-time imaging and spectroscopy we find that the host galaxy of SN 2018lfe has an absolute magnitude of $M_r = -17.85 \pm 0.24$, ($L_B = 0.029 \pm 0.007 L^*$), and an inferred metallicity of $Z \approx 0.3\ Z_\odot$ and star formation rate of $\approx 0.8\ M_\odot\ {\rm yr}^{-1}$.

Unified Astronomy Thesaurus concepts: Supernovae (1668); Core-collapse supernovae (304)

Supporting material: data behind figure

1. Introduction

Superluminous supernovae (SLSNe) are a rare class of core-collapse supernovae (SNe) that can exceed the luminosities of normal SNe by two orders of magnitude (Chomiuk et al. 2011; Quimby et al. 2011). Type I SLSNe (hereafter, SLSNe-I) are classified based on their hydrogen-free spectra, strong O II absorption lines at early times, and blue continuum (Chomiuk et al. 2011; Quimby et al. 2011; Inserra et al. 2013; Nicholl et al. 2014; Gal-Yam 2019). Despite their increasing discovery rate over the past decade thanks to systematic wide-field optical surveys, SLSNe-I still remain a small population, with only about 150 spectroscopically classified events to date (Gomez et al. 2020); moreover, not all of these events have well-observed light curves and spectroscopic time series.

Several possible mechanisms that can power SLSNe-I have been explored in the literature: large radioactive ^{56}Ni mass (Pastorello et al. 2010), circumstellar interaction (Chevalier & Irwin 2011), and a magnetar central engine (Kasen & Bildsten 2010; Woosley 2010). The bulk of the observational evidence points to a magnetar engine as the dominant mechanism. This includes the diverse light curve behavior (Nicholl et al. 2017), the early-time UV spectra (Howell et al. 2013; Mazzali et al. 2016; Nicholl et al. 2017; Yan et al. 2017; Dessart 2019), the late-time light curve flattening (Nicholl et al. 2018; Blanchard et al. 2021), and their nebular spectra (Dessart et al. 2012; Jerkstrand 2017; Nicholl et al. 2019). The preference of SLSNe-I to low metallicity host galaxies (similar to the hosts of the engine-powered long gamma-ray bursts) also supports a magnetar engine energy source (Lunnan et al. 2014; Leloudas et al. 2015; Perley et al. 2016; Chen et al. 2017; Schulze et al. 2018; Angus et al. 2019; Ørum et al. 2020).

Here, we present detailed optical observations of SN 2018lfe, a transient first detected by the Zwicky Transient Facility (ZTF; Bellm et al. 2019) on 2018 December 31 and first reported by the Pan-STARRS Survey for Transients (PSST; Chambers et al. 2019) on 2019 January 1. Our follow-up observations of the SN and its host galaxy continue up to a year after discovery and classify the event as an SLSN-I at a redshift of $z = 0.3501 \pm 0.0004$, with a peak absolute magnitude of $M_r \approx -22.1$. Our observations of the event with multiband optical observations in the g, r, w, and i bands $\approx$30 days after peak absolute magnitude and long term monitoring $\approx$100 days after peak positions it as one of the few events with multiband coverage well before peak, allowing us to better constrain its physical parameters in our models (see Section 4). We use this data set to investigate the properties of SN 2018lfe and its host, in the context of magnetar-powered SLSNe, to gain a better understanding of the larger SLSNe population.

The paper is structured as follows. In Section 2 we present SN 2018lfe and our multiband follow-up observations. In Section 3 we describe the observed features of the spectra and compare them to other SLSNe-I. In Section 4 we present our modeling of the light curve using a magnetar engine model, the bolometric light curve, and compare the parameters of SN 2018lfe to the existing SLSNe-I population. In Section 5 we explore the host galaxy properties. Throughout the paper we assume a flat ΛCDM cosmology with $H_0 = 69.3$ km s^{-1} Mpc^{-1}, $\Omega_m = 0.286$, and $\Omega_\Lambda = 0.712$ (Hinshaw et al. 2013).

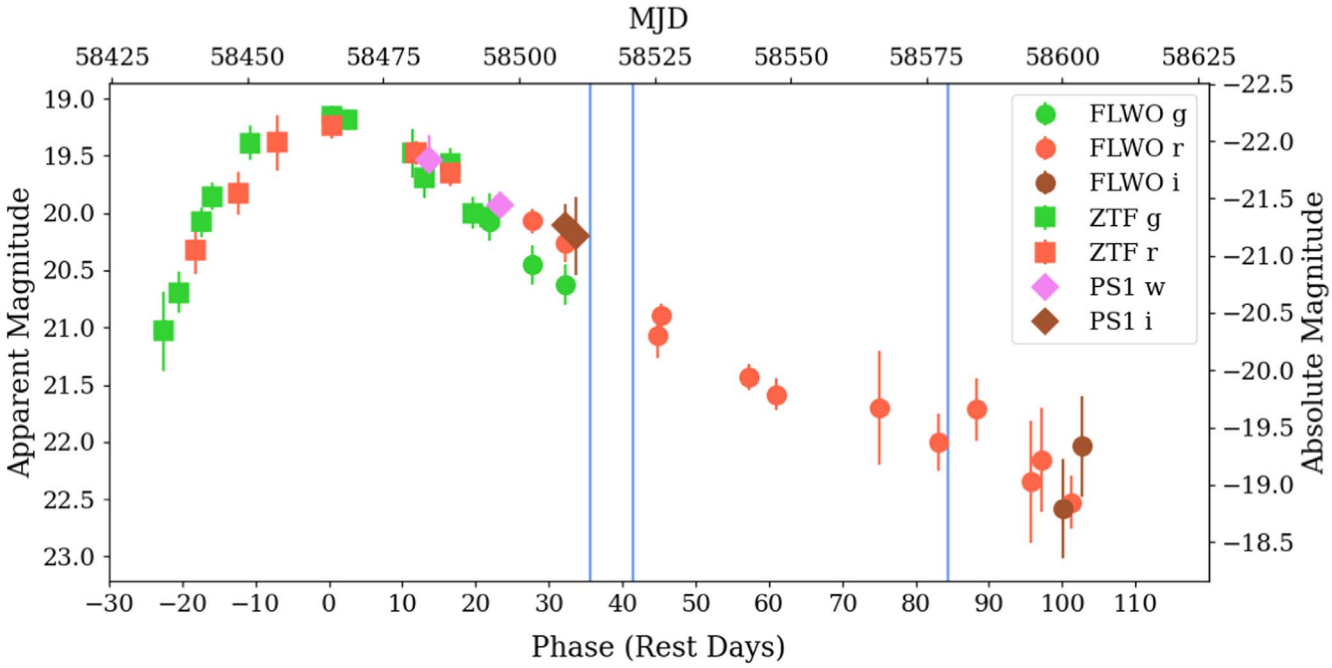

Figure 1. Optical light curve of SN 2018lfe in the *gwri* bands using data from FLWO, PSST, and ZTF. The photometry is corrected for Galactic extinction, and time is shown in rest-frame days relative to the time of peak brightness in the *r* band. The blue vertical lines mark the times when the first three spectra were taken (see Section 3), and the date of the last spectrum is outside the range of this plot. The photometry table is provided in the supplementary materials in a machine-readable format, as well as on the Open Supernova Catalog (Guillochon et al. 2017).

(The data used to create this figure are available.)

2. Observations

2.1. Discovery and Classification

SN 2018lfe was first reported by PSST on 2019 January 1 (MJD = 58484.0) with a magnitude of $g = 19.66$ at coordinates R.A. $= 09^h33^m29^s.556$, decl. $= +00°03'08''.39$ (J2000) (Chambers et al. 2019). We selected SN 2018lfe for follow-up observations as a probable SLSN-I candidate using our Finding Luminous and Exotic Extragalactic Transients (FLEET) machine-learning pipeline (Gomez et al. 2020), which determined a probability of SN 2018lfe being an SLSN-I of $P_{\rm SLSN-I} \approx 0.71$. We obtained a spectrum on 2019 January 31 with the Inamori-Magellan Areal Camera and Spectrograph(IMACS; Dressler et al. 2011) on the Magellan Baade 6.5 m Telescope and classified it as an SLSN-I (Gomez 2019) with aid from template matching to known SN spectra with the Supernovae Identification (SNID; Blondin & Tonry 2007) program. We calculated the redshift $z = 0.3501 \pm 0.0004$ by measuring the center of the Hβ and [O III] $\lambda\lambda$4959,5007 host galaxy emission lines visible in this spectrum in addition to three additional follow-up spectra.

2.2. Optical Photometry

We obtained images of SN 2018lfe with the KeplerCam imager on the 1.2 m telescope at Fred Lawrence Whipple Observatory (FLWO) in the *g*, *r*, and *i* bands, starting on 2019 January 11 (MJD=58494). SN 2018lfe was also observed at several earlier epochs by ZTF in the *g* and *r* bands, for which we obtained the raw images from the NASA/IPAC Infrared Science Archive.[6] The SN was also observed by PSST in the *w* and *i* bands, and we obtained the photometry from the publicly available data on the Open Supernova Catalog[7] (Guillochon et al. 2017).

We processed the FLWO and ZTF images using standard IRAF[8] routines. We modeled the point-spread function from each image using reference stars and subtracted the model from the target to measure the instrumental magnitudes. We combined ZTF images obtained within ≈2 days of each other to improve the signal-to-noise ratio of the measured fluxes. Similarly, for data obtained from FLWO after a phase of 110 days (MJD = 58575), we combined images in the *r* and *i* bands that were obtained within ≈2 days of each other. For the PSST photometry, we averaged the reported magnitudes obtained on the same night.

We calibrated all the photometry relative to PS1/3π magnitudes and applied a correction for Galactic extinction with $E(B-V) = 0.033 \pm 0.001$ mag and $R_V = 3.1$ (Schlafly & Finkbeiner 2011), using the Cardelli et al. (1989) Milky Way extinction law. We define phase 0 to be the date of the brightest magnitude in the *r* band, MJD = 58465, with peak apparent magnitude of $r = 19.2 \pm 0.1$ and $g = 19.1 \pm 0.1$ after correcting for Galactic extinction. We use this reference point throughout the paper, with all days quoted in the rest frame unless otherwise specified. The full light curve of SN 2018lfe is shown in Figure 1.

[6] irsa.ipac.caltech.edu

[7] https://sne.space/

[8] IRAF is written and supported by the National Optical Astronomy Observatories, operated by the Association of Universities for Research in Astronomy, Inc. under a cooperative agreement with the National Science Foundation.

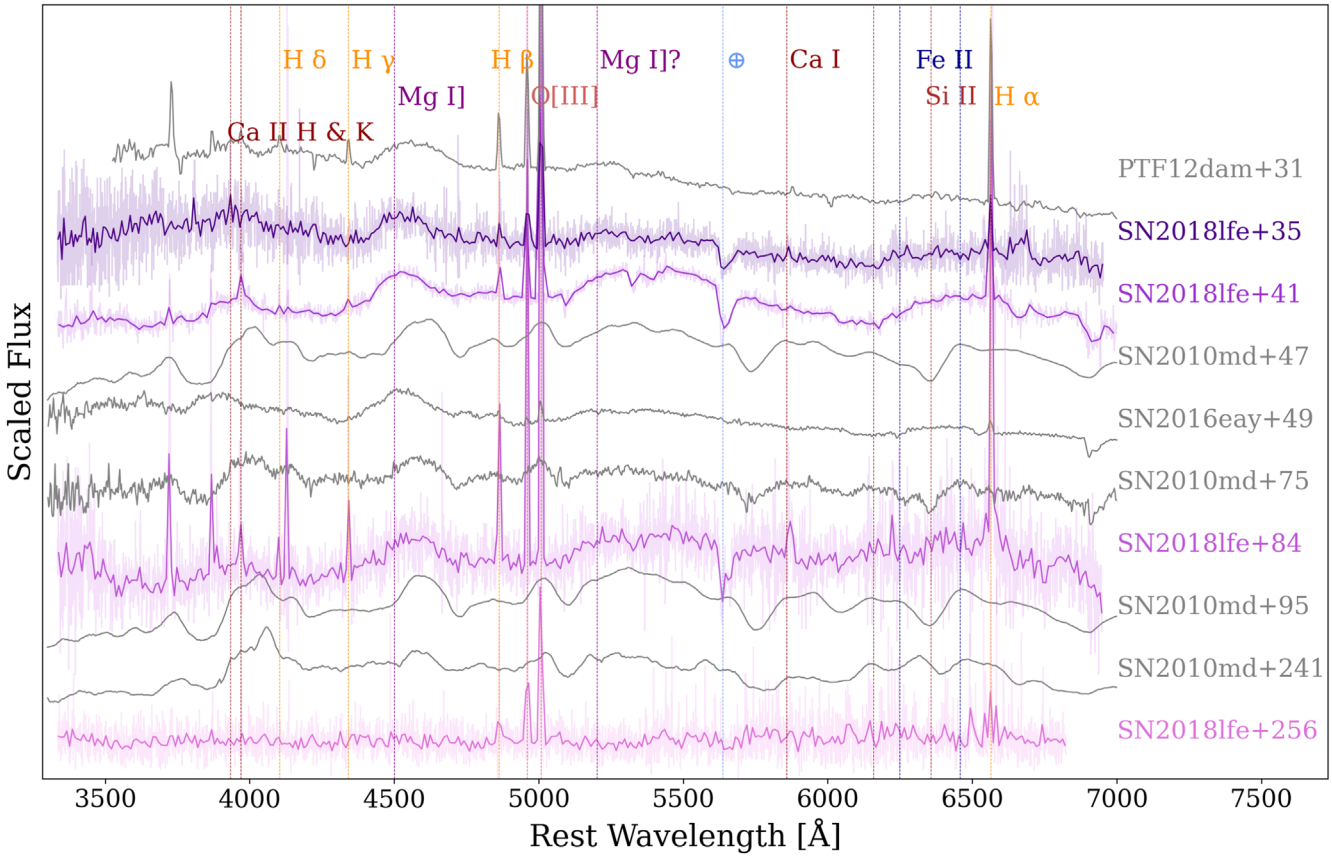

Figure 2. Optical spectra of SN 2018lfe spanning a rest-frame phase of 35–256 days, with the last spectrum being dominated by host galaxy emission. The spectra are corrected for Galactic extinction and shifted to the rest frame of SN 2018lfe using $z = 0.3501$. We bin the spectra for clarity and show the unbinned spectra as shaded regions. The labeled vertical lines mark spectral features from the SN, narrow lines from the host galaxy, and telluric absorption. The different colors in the vertical lines represent different elements. We compare the evolution of SN 2018lfe to three other SLSNe-I: SN 2010md (PTF10hgi; Inserra et al. 2013), SN 2016eay (Gaia16apd; Nicholl et al. 2017), and PTF12dam (Nicholl et al. 2013), with their spectra colored gray.

Table 1
Optical Spectroscopy of SN 2018lfe

UT Date	MJD	Phase[a] (d)	Exp. Time (s)	Airmass	Wavelength (Å)	Telescope + Instrument	Grating (lines/mm)	Slit Width (″)
2019 Jan 30	58513	35	1200	1.17	4500–9400	Baade + IMACS	300	0.9
2019 Feb 7	58521	41	1200	1.50	4500–9500	Clay + LDSS	300	1
2019 Apr 6	58579	84	1800	1.16	4500–9400	Baade + IMACS	1600	1
2019 Nov 24	58811	256	900	1.22	3800–9200	MMT + Binospec	300	0.9

Note.
[a] Rest-frame days since peak r-band luminosity.

2.3. Optical Spectroscopy

We obtained four epochs of low-resolution optical spectroscopy at phases of 35, 41, 84, and 256 days. We used the IMACS and the Low Dispersion Survey Spectrograph (LDSS3c; Stevenson et al. 2016) spectrographs on the Magellan 6.5 m telescopes and the Blue Channel (Schmidt et al. 1989) and Binospec (Fabricant et al. 2019) spectrographs on the MMT 6.5 m telescope. All the spectra were obtained with the slit oriented along the parallactic angle. Details of the spectroscopic observations are provided in Table 1.

We processed all spectra using standard IRAF routines. A wavelength calibration was applied using a HeNeAr lamp spectrum taken near the time of each science image. Relative flux calibration was applied to each spectrum using a standard star taken on the same night. The spectra were then calibrated to absolute flux scaling using the available *gri* photometry. Lastly, the spectra were corrected for Galactic extinction and transformed to the rest frame of SN 2018lfe.

The resulting spectra are shown in Figure 2, with prominent emission features from the host galaxy, absorption features of the SN, and telluric absorption features marked. The spectra are also available on the Weizmann Interactive Supernova Data Repository (WISeREP[9]; Yaron & Gal-Yam 2012).

[9] https://wiserep.weizmann.ac.il

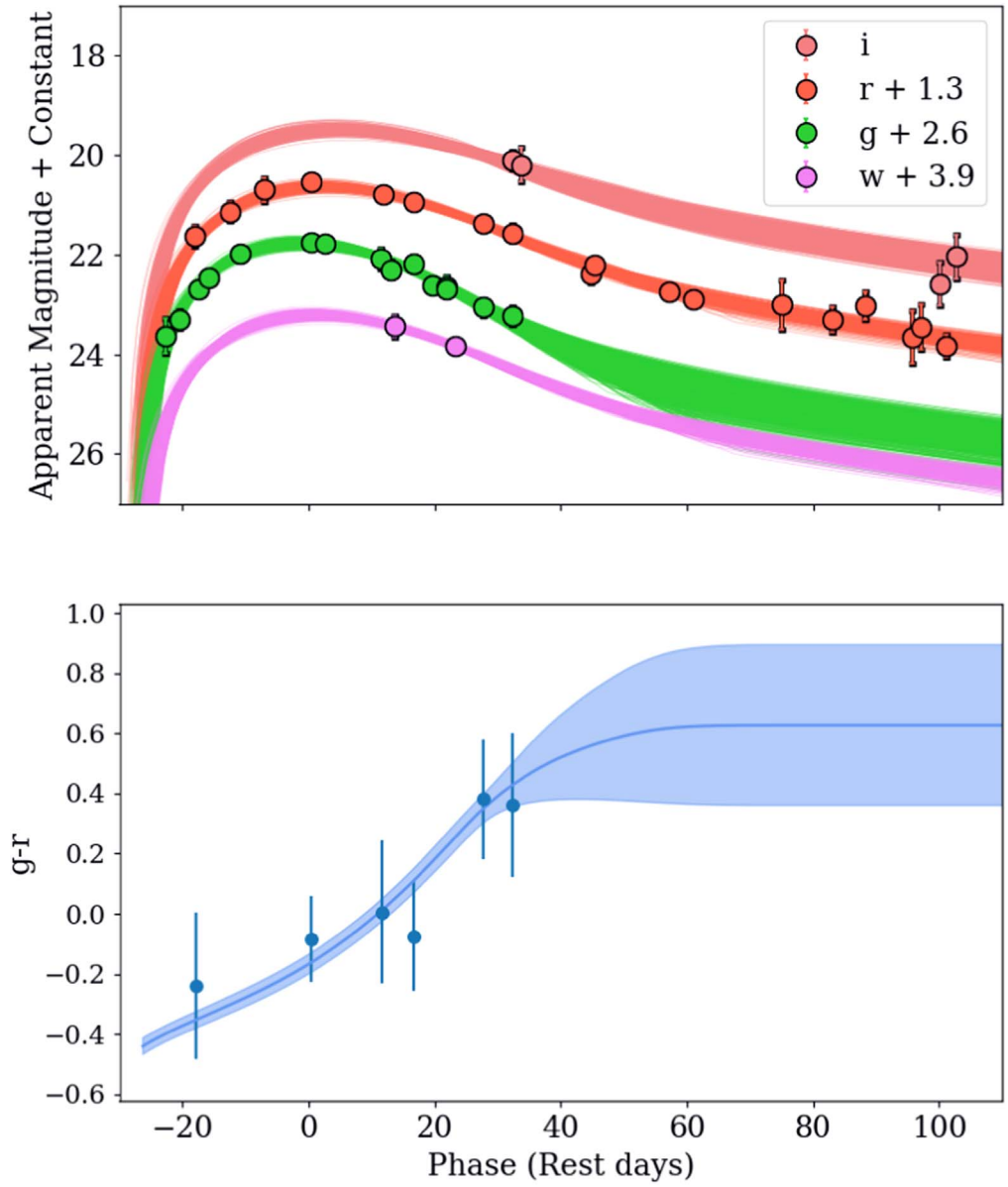

Figure 3. Top: light curve of SN 2018lfe with a magnetar engine model. Each line is a sample realization of the most likely models generated from `MOSFiT`. Bottom: color evolution (g–r) of the event. The shaded region is obtained using the `MOSFiT` light curves from the top panel. The blue data points are obtained from real observations in the g and r bands that are <1 day apart from each other.

Table 2
Best-fit Parameters for the Magnetar Models

Parameter	Definition	Prior	Full Light Curve	Units
$\log(M_{\rm ej})$	Ejecta mass	$[-1, 2]$	$0.58^{+0.11}_{-0.11}$	$M_\odot$
$B_\perp$	Magnetar magnetic field strength	[0.1, 10]	$2.8^{+2.1}_{-1.0}$	10^{14}G
$P_{\rm spin}$	Magnetar spin	[1, 10]	$2.89^{+0.47}_{-0.58}$	
$M_{\rm NS}$	Mass of neutron star	[0.1, 2.2]	$1.87^{+0.24}_{-0.41}$	$M_\odot$
$v_{\rm ej}$	Ejecta velocity	[5.0e3,2.0e4]	10062^{+867}_{-949}	km s^{-1}
E_k[a]	Ejecta kinetic energy		$3.9^{+1.3}_{-1.2}$	10^{51} erg s^{-1}
$t_{\rm exp}$	Explosion time relative to first data point	$[-500, 0]$	$-5.4^{+0.86}_{-1.0}$	days
$\log(n_{H,\rm host})$	Column density in the host galaxy	[16, 23]	$18.4^{+1.7}_{-1.7}$	cm^{-2}
$T_{\rm min}$	Photospheric temperature	[3.0e3, 1.0e4]	7683^{+1532}_{-1731}	K
κ	Optical opacity	[0.05, 0.2]	$0.16^{+0.02}_{-0.04}$	cm^{2}g^{-1}
$\log(\kappa_\gamma)$	Gamma-ray opacity	$[-1, 4]$	1.6 ± 1.6	cm^{2}g^{-1}

Note. Best model parameters, definitions, prior ranges, and 1σ error bars for the realizations shown in Figure 3.
[a] These parameters were not fit for but were calculated using all the posterior distribution samples of the fitted parameters.

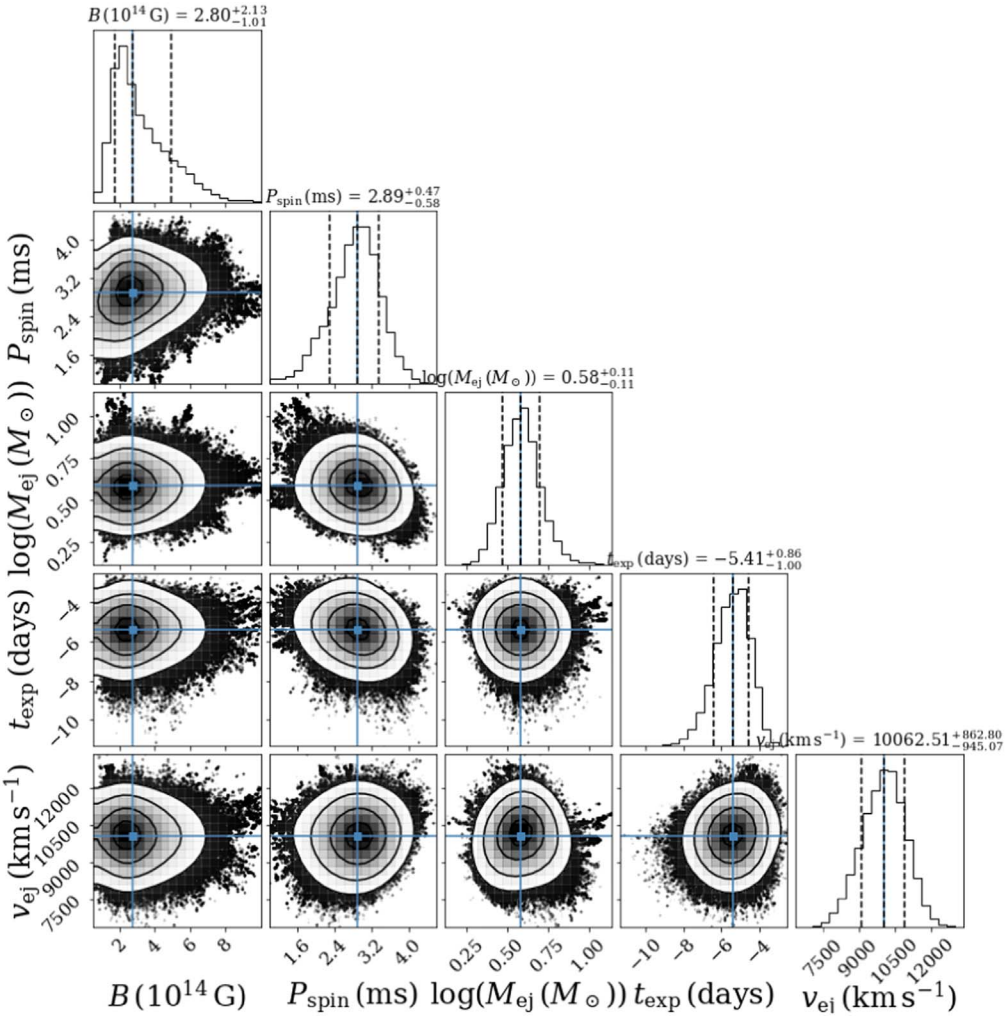

Figure 4. Posterior distributions and correlations of the magnetar model parameters. The median and 1σ values are marked and labeled. A summary of all the parameter values is presented in Table 2.

3. Spectral Features and Comparisons

The earliest spectrum of SN 2018lfe (35 days) exhibits a blue continuum and broad absorption features. We detect a broad feature at the location of]Mg I λ4500 and measure its width with a Gaussian profile, leading to velocity widths of 11190 ± 660, 11770 ± 600, and 10180 ± 470 km s^{-1} for phases of 35, 41, and 84 days, respectively. There is thus no evidence for a significant velocity evolution. The three early spectra also show Si II λ6355 regions with an average velocity center of $\approx$11,700 km s^{-1}. This is consistent with the ejecta velocity obtained from fitting the light curve with a magnetar model (see Section 4). As is common for SLSNe-I, the continuum becomes redder at later phases. No obvious SN features are detected in the final spectrum at 256 days, which shows only narrow emission lines from the host galaxy.

We compare the spectra of SN 2018lfe to those of three other SLSNe-I in Figure 2. The objects SN 2010md (=PTF10hgi) (Inserra et al. 2013), SN 2016eay (=Gaia16apd) (Nicholl et al. 2017), and PTF12dam (Nicholl et al. 2014) were chosen for having similar values of magnetar engine and ejecta parameters[10] as SN 2018lfe, and for their abundance of spectral data, specifically at phases that match those of SN 2018lfe.

The emission regions of]Mg I λ4571, Ca II H λ3933, and Ca II K λ3968 in the early spectrum of SN 2018lfe at phase of 35–41 days also match with the early phase data of SN 2010md and PTF12dam. As demonstrated in Figure 2, the spectroscopic evolution of SN 2018lfe follows that of SN 2010md. In particular, both objects display prominent Mg I] and Ca II emissions features that are similar in shape at similar phases, namely 41–47, 75–95, and 241–256 days from explosion. However, SN2010md shows an unusually prominent absorption line near 5700 Å, unlike SN 2018lfe and other typical SLSNe-I.

4. Light Curve Modeling

We model the multiband light curve with a magnetar spin-down model implemented in the Modular Open-Source Fitter for Transients (`MOSFiT`) Python package, a Markov chain Monte Carlo (MCMC) code that can fit the light curves of transients using a variety of power sources (Guillochon et al. 2018). Note that an attempt using the nickel–cobalt decay model displays a high nickel fraction $F_{\rm Ni} \approx 0.9$ ($M_{\rm Ni} = 25\,M_\odot$) inconsistent with the blue colors of the spectra, as seen from the spectral observations, since

[10] The values of these parameters are from our previous work in Nicholl et al. (2017).

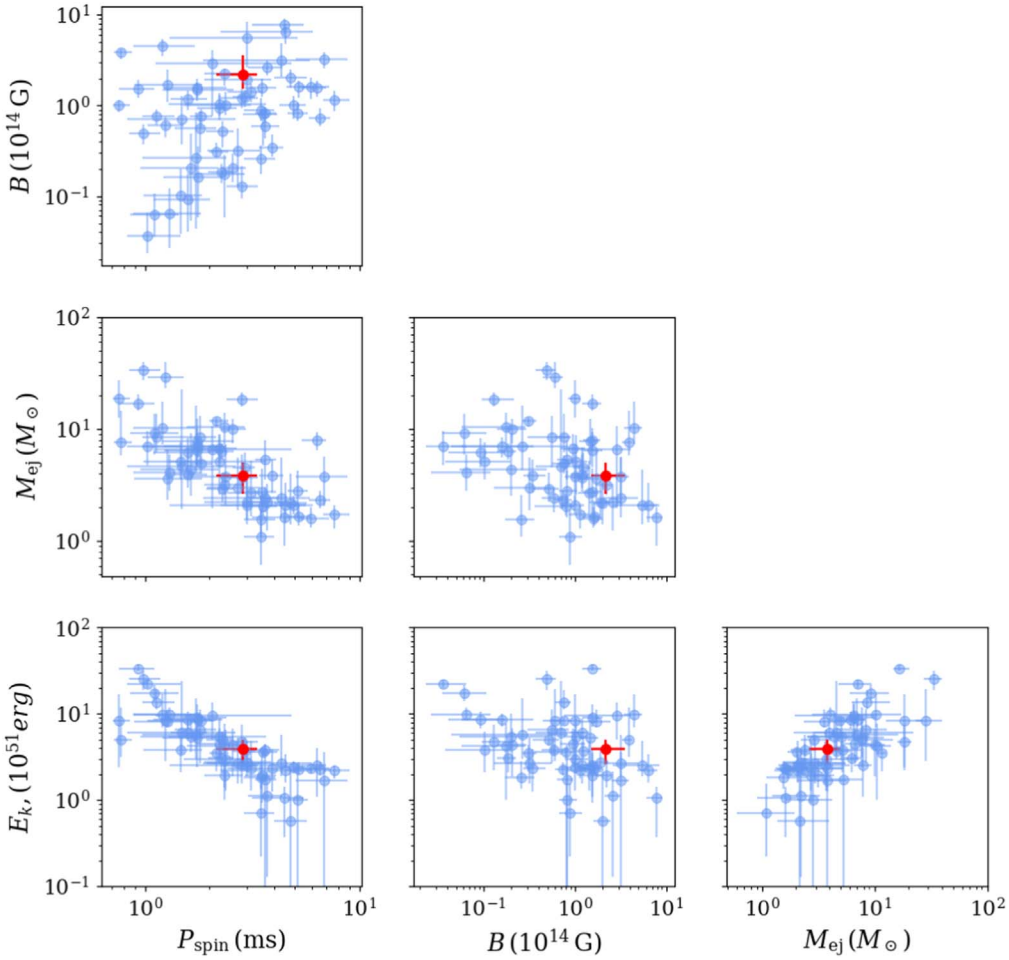

Figure 5. Median values and 1σ errors of key parameters (P, $B_\perp$, M_{ej}, E_K) for all SLSNe in Villar et al. (2018), Nicholl et al. (2015), and Blanchard et al. (2020) (labeled blue) compared with SN 2018lfe (labeled orange). SN 2018lfe lies consistent with the magnetar model.

Table 3
Host Galaxy Properties

	Value (mag)	Units
g	24.07 ± 0.20	mag
r	23.52 ± 0.24	mag
i	24.01 ± 0.19	mag
z	24.36 ± 0.19	mag
M_g	-17.30 ± 0.2	mag
M_r	-17.85 ± 0.3	mag
M_i	-17.36 ± 0.4	mag
M_z	-17.01 ± 0.3	mag
L_B	0.029 ± 0.01	L^*
$12 + \log(\mathrm{O/H})$	8.18 ± 0.12	
Z	0.31 ± 0.05	$Z_\odot$
SFR	0.77 ± 0.02	$M_\odot\ \mathrm{yr}^{-1}$

Note. Apparent magnitudes, not corrected for extinction, obtained from observations using the Binospec (Fabricant et al. 2003) imaging camera on the MMT on 2020 November 15. Absolute magnitudes are corrected for extinction. The star formation rate (SFR) and the metallicities (in terms of $12 + \log(\mathrm{O/H})$ and $Z_\odot$) are estimated using the flux immensities of the host galaxy emission lines. L_B is the host luminosities relative to L^* in the B band (Willmer et al. 2006). Due to the fact that at $z = 0.35$, the observed r band is closest to rest-frame B band; see Section 5.

nickel-rich SNe are expected to have heavy line-blanketing and red spectral colors (e.g., see Darbha et al. 2010; Dessart et al. 2012). Added: the radiated energy predicted by the radioactive decay model is $\approx 3.9 \times 10^{51}$erg s^{-1}, consistent with the magnetar model. But if the energy is produced purely from nickel decay, this would require a specific set of mixing and asymmetry conditions to be consistent with the blue spectra and the lack of line blanketing (Quimby et al. 2007). Hydrodynamical simulations would be required to test whether these conditions are possible, and these simulations are outside the scope of this paper. The model is therefore depreciated. Although the effects of fitting spherical models, such as ones used in `MOSFIT`, to nonspherical SLSN explosions is not yet well understood, it has been shown that using a nonspherical model makes little difference in Type Ic SNe and thus SLSNe progenitor models (Afsariardchi & Matzner 2018). We use the `emcee` (Foreman-Mackey et al. 2013) implementation of MCMC to run each sampler. Since `MOSFiT` implements a simplified analytical one-zone model, the uncertainties presented here represent only the statistical errors on the fit. The priors used in the model are listed in Table 2, following our previous work in Nicholl et al. (2017).

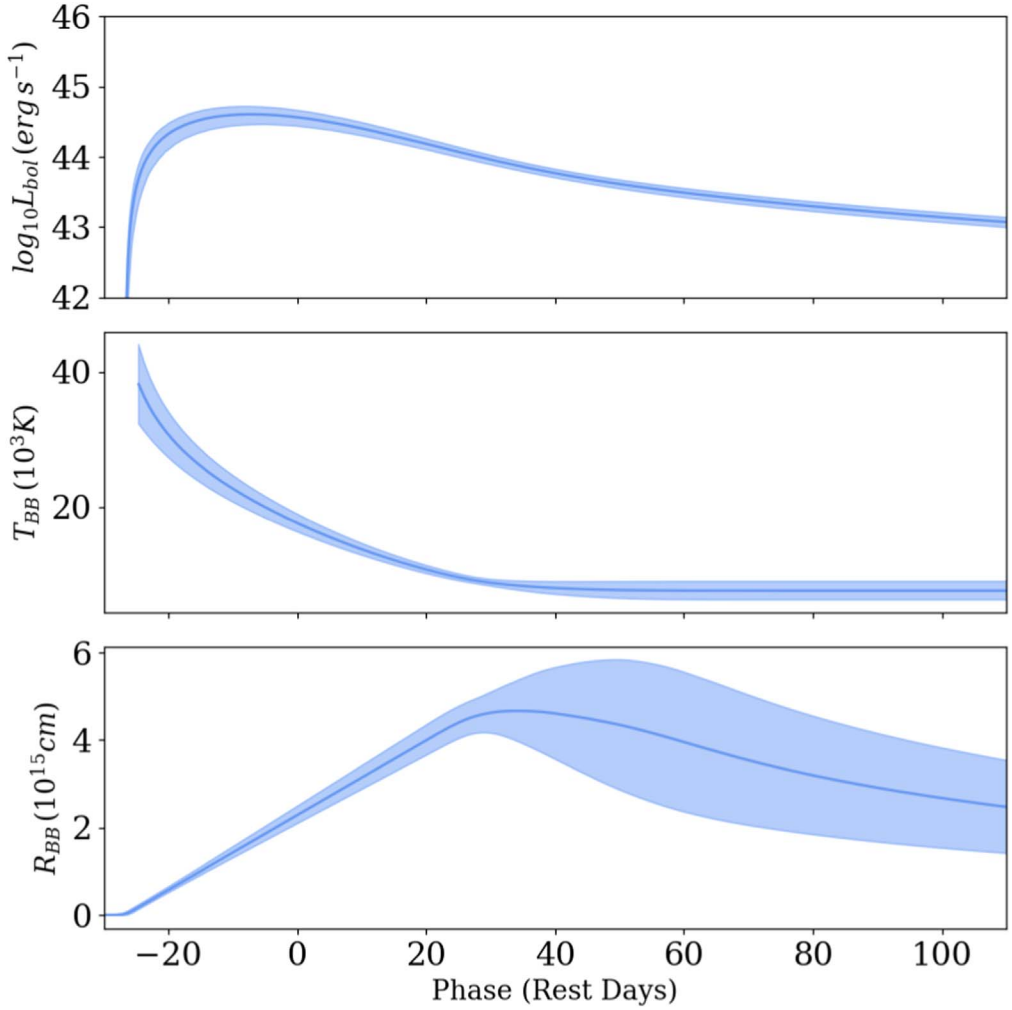

Figure 6. Bolometric light curve, blackbody temperature evolution, and photospheric radius evolution obtained from the MOSFiT models. The plots show the mean model (blue line) and the 1σ regions of 500 walkers used in the MCMC process.

The magnetar model fits are shown in Figure 3, and the parameter posterior distributions are shown in Figure 4 and listed in Table 2. The model provides an excellent fit to the data, with the following primary physical parameters: an initial spin period of $P \approx 2.9$ ms, a magnetic field of $B_{\perp} \approx 2.8 \times 10^{14}$ G, an ejecta mass of $M_{\rm ej} \approx 3.8\ M_{\odot}$, and an ejecta velocity of $v_{\rm ej} \approx 10^4$ km s^{-1} (in good agreement with the velocity inferred from the spectra in Section 3). We calculate a total kinetic energy of $E_K \approx 4 \times 10^{51}$ erg. The mass of the progenitor star is estimated to be $M_{\rm NS} + M_{\rm ej} \approx 5.7\ M_{\odot}$, which is consistent with the range of 3.6–40 $M_{\odot}$ inferred from the SLSNe-I sample of Blanchard et al. (2020).

We compare the resulting parameters for SN 2018lfe to the distribution of 62 SLSNe from Nicholl et al. (2015), Blanchard et al. (2020), and Villar et al. (2018) in Figure 5. As seen in the figure, all of the parameters for SN 2018lfe fall within the range covered by previous SLSNe. However, we do find that the magnetic field value inferred for SN 2018lfe is in the top 16$^{\rm th}$ percentile of the SLSN distribution. The combination of the strong magnetic field, fast spin ($P_{\rm spin} < 3$ ms), and high ejecta velocity is most likely responsible for the significant heating of the ejecta, which explains the high optical luminosity of SN 2018lfe.

We further use the MOSFiT model to construct a bolometric light curve, photospheric radius evolution, and temperature evolution of SN 2018lfe; see Figure 6. The shaded regions in the figure represent the 1σ values across all 500 walkers. We find a peak bolometric luminosity of $(4.0 \pm 1.1) \times 10^{44}$ erg s^{-1}. The integrated radiated energy over the observed portion of the light curve (phase 0–103 days) is $E_{\rm rad} \approx 1.2 \times 10^{51}$ erg, consistent with the known population of SLSNe, despite its bright peak luminosity (Lunnan et al. 2018; Nicholl et al. 2020). The error bars presented here represent only the statistical uncertainties of the fits. Understanding the full systematics of the MOSFiT model would require full hydrodynamical simulations and is thus outside the scope of this paper. The photospheric radius exhibits an increase up to a maximum of $4.6^{+1.1}_{-0.5} \times 10^{15}$ cm at a phase of $\approx$30–50 days, with a gradual decline thereafter. Finally, the photospheric temperature shows a steady decline from an inferred peak of $\approx 3.5 \times 10^4$ K down to $\approx 10^4$ K at a phase of $\gtrsim$30 days and suggests a temperature $< 10^4$ K at 40 days. Although due to the lack of data in the UV range, there is large uncertainty at early times when the spectral energy distribution peaks in this wavelength range.

5. Host Galaxy

No galaxy is detected at the position of SN 2018lfe in the PS1/3π catalog down to the nominal 5σ limiting magnitudes of $g \approx 23.3$, $r \approx 23.2$, $i \approx 23.1$, and $z \approx 22.3$ (Chambers et al. 2016). We obtained deeper images on 2020 November 15 using Binospec and detected an extended source with a half-light radius of $\approx 0\farcs5$, measured using `sep` (Barbary et al. 2015). From extrapolating the observed light curve (see Section 2.2), we expect the apparent magnitude of the SLSN to be dimmer than ≈25 mag in the r band, therefore the host should be the only source present. We extracted the host magnitudes by performing aperture photometry using the `photutils` package (Bradley et al. 2020) with a circular aperture of radius $2''$ across all filters. At the measured redshift of $z = 0.3501$, the observed r band is closest to the rest-frame B band. The apparent host magnitude of $r = 23.52 \pm 0.24$ mag thus corresponds to a $L_B = 0.029 \pm 0.007\ L^*$, determined using the DEEP2 luminosity function at $z = 0.3$ (Willmer et al. 2006). The host galaxy properties are summarized in Table 3.

We measured the strength of the galaxy emission lines by fitting narrow Gaussian profiles (FWHM ≈ 40Å) to the three spectra at phases of 35, 41, and 84 days. The flux ratio of $L_{\mathrm{H}\alpha}/L_{\mathrm{H}\beta} = 2.75 \pm 0.37$ is consistent with the expectation for case B recombination ($L_{\mathrm{H}\alpha}/L_{\mathrm{H}\beta} = 2.86$), suggesting no significant host galaxy extinction (in agreement with the lack of extinction inferred from modeling of the SN light curves). The Hα line luminosity is $L_{\mathrm{H}\alpha} = (9.8 \pm 0.3) \times 10^{43}$ erg s^{-1}. This corresponds to a star formation rate of $0.77 \pm 0.02\ M_\odot$ yr^{-1} (Kennicutt 1998)

To calculate the metallicity we use the R_{23} method (Kobulnicky et al. 1999) and adopt the lower branch solution due to the lack of an N II detection. We determine a value of $12 + \log(\mathrm{O/H}) = 8.18 \pm 0.12$, or $Z = 0.31 \pm 0.05\ Z_\odot$ (Asplund et al. 2009). Coincidentally, this is also where the two values from the R_{23} method converge, and therefore our metallicity is not affected by the choice of the lower or upper branch solution. The low metallicity is consistent with the consensus that SLSNe preferentially occur in galaxies with subsolar metallicity (Lunnan et al. 2014; Perley et al. 2016; Chen et al. 2017; Schulze et al. 2017).

6. Conclusions

We presented the classification and detailed optical follow-up observations of the Type I SLSN 2018lfe and its host galaxy at $z = 0.3501 \pm 0.0004$. We model the light curve using a spin-down magnetar model and find that SN 2018lfe has a best-fit ejecta mass of $\approx 3.8\ M_\odot$, a magnetar spin period of ≈2.9 ms, and a magnetic field strength of $\approx 2.8 \times 10^{14}$ G, consistent with the population of known SLSNe. We determine the host galaxy properties through spectral analysis and follow-up photometric observations, and find a low metallicity of $12 + \log(\mathrm{O/H}) = 8.18 \pm 0.12$, typical for SLSNe-I hosts. Therefore, SN 2018lfe is a typical SLSN-I in terms of its explosion and host galaxy properties and contributes to a small population of SLSNe-I with a well-defined explosion time and peak absolute magnitude.

We thank Y. Beletsky for carrying out some of the Magellan observations. The Berger Time-Domain Group at Harvard is supported in part by NSF under grant AST-1714498 and by NASA under grant NNX15AE50G. M. Nicholl is supported by a Royal Astronomical Society Research Fellowship and by the European Research Council (ERC) under the European Unions Horizon 2020 research and innovation program (grant agreement No. 948381). Operation of the Pan-STARRS1 telescope is supported by the National Aeronautics and Space Administration under grant No. NNX12AR65G and grant No. NNX14AM74G issued through the NEO Observation Program. This paper includes data gathered with the 6.5 m Magellan Telescopes located at Las Campanas Observatory, Chile. Observations reported here were obtained at the MMT Observatory, a joint facility of the University of Arizona and the Smithsonian Institution. This research has made use of NASA's Astrophysics Data System. This research has made use of the SIMBAD database, operated at CDS, Strasbourg, France.

Software: Astropy (Astropy Collaboration et al. 2018), MOSFiT (Guillochon et al. 2018), PyRAF (Science Software Branch at STScI 2012), SAOImage DS9 (Smithsonian Astrophysical Observatory 2000), emcee (Foreman-Mackey et al. 2013), corner (Foreman-Mackey 2016), Matplotlib (Hunter 2007), SciPy (van der Walt et al. 2011), NumPy (Oliphant 2007), SEP (Barbary et al. 2015) extinction (Barbary 2016), FLEET (Gomez et al. 2020)).

ORCID iDs

Yao Yin https://orcid.org/0000-0002-5723-8023
Sebastian Gomez https://orcid.org/0000-0001-6395-6702
Edo Berger https://orcid.org/0000-0002-9392-9681
Griffin Hosseinzadeh https://orcid.org/0000-0002-0832-2974
Matt Nicholl https://orcid.org/0000-0002-2555-3192
Peter K. Blanchard https://orcid.org/0000-0003-0526-2248

References

Afsariardchi, N., & Matzner, C. D. 2018, ApJ, 856, 146
Angus, C. R., Smith, M., Sullivan, M., et al. 2019, MNRAS, 487, 2215
Asplund, M., Grevesse, N., Sauval, A. J., & Scott, P. 2009, ARA&A, 47, 481
Astropy Collaboration, Price-Whelan, A. M, Sipőcz, B. M., et al. 2018, AJ, 156, 123
Barbary, K. 2016, extinction, v0.3.0, Zenodo, doi:10.5281/zenodo.804967
Barbary, K., Boone, K., & Deil, C. 2015, sep: v0.3.0, v0.3.0, Zenodo, doi:10.5281/zenodo.15669
Bellm, E. C., Kulkarni, S. R., Graham, M. J., et al. 2019, PASP, 131, 018002
Blanchard, P. K., Berger, E., Nicholl, M., et al. 2021, ApJ, 921, 64
Blanchard, P. K., Berger, E., Nicholl, M., & Villar, V. A. 2020, ApJ, 897, 114
Blondin, S., & Tonry, J. L. 2007, ApJ, 666, 1024
Bradley, L., Sipőcz, B., Robitaille, T., et al. 2020, astropy/photutils: 1.0.0, 1.0.0, Zenodo, doi:10.5281/zenodo.4044744
Cardelli, J. A., Clayton, G. C., & Mathis, J. S. 1989, ApJ, 345, 245
Chambers, K. C., Magnier, E. A., Metcalfe, N., et al. 2016, arXiv:1612.05560
Chambers, K. C., Huber, M. E., Flewelling, H., et al. 2019, Transient Name Server Discovery Report, 2019-5, 1
Chen, T.-W., Schady, P., Xiao, L., et al. 2017, ApJL, 849, L4
Chevalier, R. A., & Irwin, C. M. 2011, ApJL, 729, L6
Chomiuk, L., Chornock, R., Soderberg, A. M., et al. 2011, ApJ, 743, 114
Darbha, S., Metzger, B. D., Quataert, E., et al. 2010, MNRAS, 409, 846
Dessart, L. 2019, A&A, 621, A141
Dessart, L., Hillier, D. J., Waldman, R., Livne, E., & Blondin, S. 2012, MNRAS, 426, L76
Dressler, A., Bigelow, B., Hare, T., et al. 2011, PASP, 123, 288
Fabricant, D., Fata, R., Epps, H., et al. 2019, PASP, 131, 075004
Fabricant, D. G., Epps, H. W., Brown, W. L., Fata, R. G., & Mueller, M. 2003, Proc. SPIE, 4841, 1134
Foreman-Mackey, D. 2016, JOSS, 1, 24
Foreman-Mackey, D., Hogg, D. W., Lang, D., & Goodman, J. 2013, PASP, 125, 306
Gal-Yam, A. 2019, ARA&A, 57, 305

Gomez, S. 2019, Transient Name Server Classification Report, 2019-1246, 1
Gomez, S., Berger, E., Blanchard, P. K., et al. 2020, ApJ, 904, 74
Gomez, S., Berger, E., Blanchard, P. K., et al. 2020, FLEET Finding Luminous and Exotic Extragalactic Transients, v1.0.0, Zenodo, doi:10.5281/zenodo.4013965
Guillochon, J., Nicholl, M., Villar, V. A., et al. 2018, ApJS, 236, 6
Guillochon, J., Parrent, J., Kelley, L. Z., & Margutti, R. 2017, ApJ, 835, 64
Hinshaw, G., Larson, D., Komatsu, E., et al. 2013, ApJS, 208, 19
Howell, D. A., Kasen, D., Lidman, C., et al. 2013, ApJ, 779, 98
Hunter, J. D. 2007, CSE, 9, 90
Inserra, C., Smartt, S. J., Jerkstrand, A., et al. 2013, ApJ, 770, 128
Jerkstrand, A. 2017, Handbook of Supernovae (Cham: Springer), 795
Kasen, D., & Bildsten, L. 2010, ApJ, 717, 245
Kennicutt, R. C. J. 1998, ARA&A, 36, 189
Kobulnicky, H. A., Kennicutt, R. C. J., & Pizagno, J. L. 1999, ApJ, 514, 544
Leloudas, G., Schulze, S., Krühler, T., et al. 2015, MNRAS, 449, 917
Lunnan, R., Chornock, R., Berger, E., et al. 2014, ApJ, 787, 138
Lunnan, R., Fransson, C., Vreeswijk, P. M., et al. 2018, NatAs, 2, 887
Mazzali, P. A., Sullivan, M., Pian, E., Greiner, J., & Kann, D. A. 2016, MNRAS, 458, 3455
Nicholl, M., Berger, E., Blanchard, P. K., Gomez, S., & Chornock, R. 2019, ApJ, 871, 102
Nicholl, M., Berger, E., Margutti, R., et al. 2017, ApJL, 835, L8
Nicholl, M., Guillochon, J., & Berger, E. 2017, ApJ, 850, 55
Nicholl, M., Smartt, S. J., Jerkstrand, A., et al. 2013, Natur, 502, 346
Nicholl, M., Smartt, S. J., Jerkstrand, A., et al. 2014, MNRAS, 444, 2096
Nicholl, M., Smartt, S. J., Jerkstrand, A., et al. 2015, ApJL, 807, L18
Nicholl, M., Blanchard, P. K., Berger, E., et al. 2018, ApJL, 866, L24
Nicholl, M., Blanchard, P. K., Berger, E., et al. 2020, NatAs, 4, 893
Oliphant, T. E. 2007, CSE, 9, 10
Ørum, S. V., Ivens, D. L., Strandberg, P., et al. 2020, A&A, 643, A47
Pastorello, A., Smartt, S. J., Botticella, M. T., et al. 2010, ApJL, 724, L16
Perley, D. A., Quimby, R. M., Yan, L., et al. 2016, ApJ, 830, 13
Quimby, R. M., Aldering, G., Wheeler, J. C., et al. 2007, ApJL, 668, L99
Quimby, R. M., Kulkarni, S. R., Kasliwal, M. M., et al. 2011, Natur, 474, 487
Schlafly, E. F., & Finkbeiner, D. P. 2011, ApJ, 737, 103
Schmidt, G. D., Weymann, R. J., & Foltz, C. B. 1989, PASP, 101, 713
Schulze, S., Krühler, T., Leloudas, G., et al. 2017, MNRAS, 473, 1258
Schulze, S., Krühler, T., Leloudas, G., et al. 2018, MNRAS, 473, 1258
Science Software Branch at STScI 2012, PyRAF: Python alternative for IRAF, Astrophysics Source Code Library, ascl:1207.011
Smithsonian Astrophysical Observatory 2000, SAOImage DS9: A utility for displaying astronomical images in the X11 window environment, Astrophysics Source Code Library, ascl:0003.002
Stevenson, K. B., Bean, J. L., Seifahrt, A., et al. 2016, ApJ, 817, 141
van der Walt, S., Colbert, S. C., & Varoquaux, G. 2011, CSE, 13, 22
Villar, V. A., Nicholl, M., & Berger, E. 2018, ApJ, 869, 166
Willmer, C. N. A., Faber, S. M., Koo, D. C., et al. 2006, ApJ, 647, 853
Woosley, S. E. 2010, ApJL, 719, L204
Yan, L., Lunnan, R., Perley, D. A., et al. 2017, ApJ, 848, 6
Yaron, O., & Gal-Yam, A. 2012, PASP, 124, 668